Ni Migration of Fuel Electrode in Solid Oxide Electrolysis Cell: An Integrated Model Study

Yang Wang[a,b], Chengru Wu[a,b], Bingfeng Zu[c], Minfang Han[d], Qing Du[a,*], Meng Ni[b,*], Kui Jiao[a,*]

[a]State Key Laboratory of Engines, Tianjin University,

135 Yaguan Road, Tianjin, China, 300350

[b]Department of Building and Real Estate,

Hong Kong Polytechnic University, Hung Hom, Kowloon, Hong Kong, China

[c]Internal Combustion Engine Research Institute, Tianjin University, 92 Weijin Road, Tianjin， China

[d]Department of Energy and Power Engineering, Tsinghua University, Beijing, Beijing, 100084, China

*Corresponding author: duqing@tju.edu.cn (Q. Du); meng.ni@polyu.edu.hk (M. Ni); kjiao@tju.edu.cn (K. Jiao)

Abstract

During the long-term operation of solid oxide electrolysis cell (SOEC), the coarsening and depletion of the Ni phase of the electrode are found to decrease the cell performance and limit cell durability. In this study, a comprehensive numerical study is conducted to quantitatively evaluate the degradation process in the fuel electrode of SOEC. The phase-field model is adopted to track the Ni phase migration process and generate the electrode structures with Ni depletion. An electrode model based on the lattice Boltzmann method is then used to evaluate the electrochemical performance of the fuel electrode. It is found that the maximum width of

the Ni depletion region can reach 3-4 μm. The Ni depletion will aggravate the coarsening of the Ni phase. The corresponding electrochemical evaluation also shows that the randomly distributed ionic particles in the porous fuel electrode lengthens the ion transport path and increases the electrode ohmic overpotential. The Ni depletion also increases the activation overpotential loss due to the reduction of the active reaction sites. The severe Ni depletion can increase the total overpotential by up to 52.8% compared to the initial state. Besides, increasing the wettability of the Ni phase can effectively suppress the reduction of active reaction sites due to Ni coarsening.

Keywords: SOEC, Ni depletion, Phase-field model, Lattice Boltzmann model, Cell performance.

Nomenclature

C	conserved order parameters
C_{H_2}	molar concentration (mol m^{-3})
d_p	average diameter of pore (μm)
$D_{i,k}$	Knudsen diffusion coefficients (m^2 s^{-1})
$D_{i,j}$	binary diffusion coefficients (m^2 s^{-1})
E_{act}	activation energy (J mol^{-1})
F	the Faraday constant (C mol^{-1})
F_{total}	total free energy of the system

f_0	bulk free energy density
J	electrochemical reaction rate (A m^{-3} s^{-1})
j_0	exchange current density (A m^{-3})
L	mobility of non-conserved order parameters
L_{TPB}	local TPB density (μm $μm^{-3}$)
l_0	characteristic length (nm)
M	average molar mass (kg mol^{-1})
M_C	mobility of conserved order parameters
n_e	number of electrons transferred per reaction
P	pressure (Pa)
p	partial pressure (Pa)
T	temperature (K)
t_0	characteristic time (h)
V_i	special Fuller diffusion volume (cm^{-3} mol^{-1})
W_{ca}	Wettability parameter

Greek letters

γ_a	adjustable parameter
φ	electric potential (V）
η_i	non-conserved order parameters
η_{act}	activation overpotential

κ	gradient energy coefficients
σ	conductivity (S m^{-1})
ω_i	weight coefficients
τ_i	relaxation coefficients

Subscripts and superscripts

act	activation
bulk	Bulk diffusion
ele	electron
ion	ion
N	Ni
Y	YSZ
P	pore

Abbreviations

CGO	gadolinium-doped ceria
LBM	lattice Boltzmann method
MRT	multiple-relaxation-time
PFM	phase-field model
SOCs	Solid oxide cells
SOEC	solid oxide electrolysis cell
SOFC	solid oxide fuel cell

TPB	three-phase boundaries
TPBl	three-phase boundaries length
YSZ	yttria stabilized zirconia

1. Introduction

Nowadays, the share of renewable energy in the world's energy system is steadily rising [1]. The rapid development of solar, wind, and tidal energy provides a variety of large-scale available electric power resources and is expected to solve the environmental and climate change problems caused by the use of fossil fuels [2]. Electrolysis technology, which converts renewable electricity into chemical energy for fuel, plays a critical role in storing excess renewable power in the form of chemical energy [3]. The produced fuels can then be used in fuel cells for power generation. Among various electrolysis devices, solid oxide electrolysis cell (SOEC) is considered as a promising technology for large scale electrolysis of water or CO_2 [4].

SOEC can be operated reversibly, and the cell can be switched between electrolysis and fuel cell (SOFC) modes. Stable operational life is a prerequisite for solid oxide cells (SOCs) to be commercially available on a large scale [5]. Normally the degradation rate of a cell should be limited to 0.5%/kh for a long-term operation to be commercially viable, but at this stage most long-term tests still do not meet this requirement especially for SOEC [6]. The performance degradation of SOCs is determined by the joint effects of cell materials, fabrication processes,

and operating conditions [7]. Among them, microscopic morphological evolution of fuel electrodes during operation is a main reason for cell performance degradation [8]. For conventional SOCs, the fuel electrode is usually a composite of Ni and ceramic material, such as yttria-stabilized zirconia (YSZ) and gadolinium-doped ceria (CGO). The Ni phase tends to change morphology under high-temperature operating conditions, which in turn leads to irreversible loss of cell performance [9].

The most common electrode microstructure evolution during cell operation is Ni coarsening, especially at high operating temperature. The high operating temperature of SOCs makes the Ni phase more inclined to sintering. The initial microstructure has a smaller Ni particle size and larger surface energy. The tendency to reduce the total system free energy causes the Ni particles to aggregate to reduce the surface energy [10]. This results in a rapid increase in Ni particle size in the early stage. The direct consequence of the rapid increase of Ni particle size is the decrease of the three-phase boundaries (TPB) length, which reduces the active reaction sites and increases the activation overpotential. Ni coarsening is a common phenomenon in both fuel cell and electrolysis cell modes [11]. Meanwhile, in many long-term tests, SOEC showed another nickel migration process that is not evident in the fuel cell mode. The Ni phase migrates from the region close to the electrolyte towards the surface of the electrode. This process leads to a more severe Ni depletion n1ear electrolyte, which further decreases the cell performance. This phenomenon exists in electrodes of different materials such as Ni-YSZ and Ni-CGO, as well as in electrolysis cells with different geometries such as fuel electrode-supported and electrolyte-supported configurations [12-14]. Fig. 1(a) shows the schematic of

the Ni migration process in the Ni-YSZ electrode.

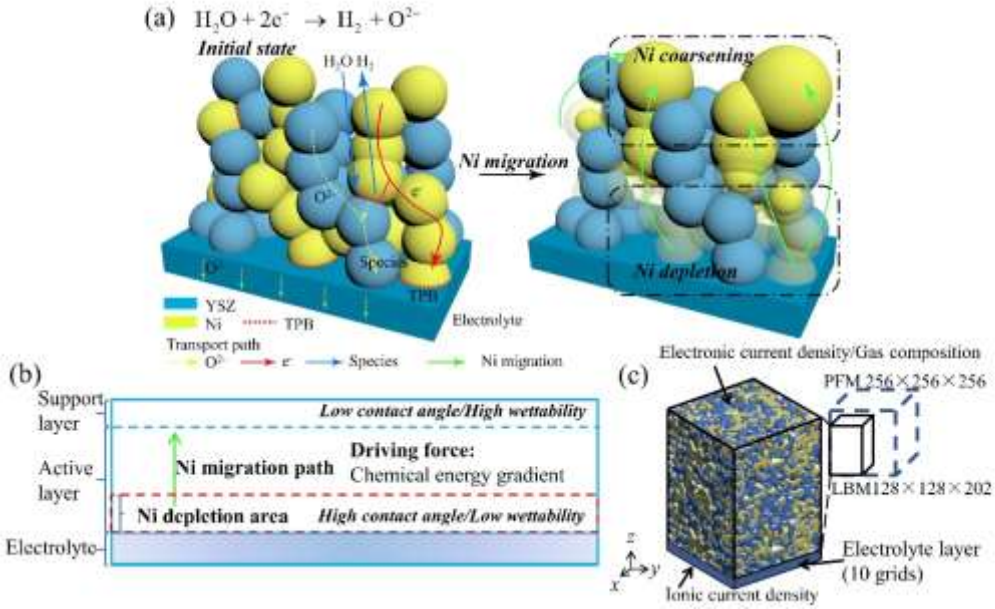

Fig. 1. (a) The schematic of the Ni migration process in the fuel electrode, (b) The mechanism of Ni migration [19], (c) Computational domain and boundary conditions.

The Ni depletion is mainly driven by the operating current density, and the degree of depletion is a complex combination of overpotential, humidity, and temperature. It is more pronounced when the steam volume fraction is larger than 0.8 and temperature is above 800 °C [15]. For planar cells, the degree of Ni depletion at the inlet and outlet of the fuel electrode can differ significantly [16]. This indicates that the degree of Ni depletion depends to a large extent on local humidity. In addition, Ni depletion can also occur in co-electrolysis mode of water and CO_2, and it is a non-negligible phenomenon not only at high but also at moderate current density (~5000 $A \cdot m^{-2}$) [17]. Some hypotheses on the mechanism of Ni depletion have been

proposed [18,19]. Mogenson et al. [18] attributed the migration process to the formation of $Ni(OH)_x$ volatile species which diffuse along the water pressure gradient. Trini et al. [19] proposed an alternative hypothesis: Ni migration is driven by the oxygen potential gradient which leads to the variation of the contact angle between Ni and YSZ phases. In conclusion, Ni depletion can have a great impact on the durability of SOEC and still needs further study. However, only experimental studies on Ni coarsening during long-term operation have been reported [20-22], while no simulation study on Ni depletion can be found in the literature. Numerical modeling is cost effective and can provide insights in the Ni depletion process, thus it is highly desirable to conduct a modeling study on SOC with a focus on the Ni depletion and coarsening processes. Some numerical models have been developed to study Ni coarsening in fuel cell mode [23-25]. Compare to the analytical and empirical models, the phase-field model (PFM) has been shown to capture the morphological evolution of the real electrode very well. Based on thermodynamic theory, the PFM can effectively capture the evolution of the continuous phase interface. Li et al. [23] first applied the PFM to simulate the evolution of the SOFC anode microstructure. Jiao et al. [25] experimentally reconstructed the initial microstructure and quantitatively investigated several factors affecting the durability of the electrodes based on the PFM. Wang et al. [10] had applied a PFM to quantitatively analyze the effects of Ni coarsening on the morphology and performance evolution of fuel electrodes in SOFC. These findings have demonstrated that the PFM has a good fit for the simulation on the evolution of the three-phase SOCs electrodes.

The study on Ni migration, especially Ni depletion, is essential to improve the long-term

stability of SOEC. The effect of Ni depletion on the microstructure morphology and cell performance needs to be further quantified. As there is no modeling study on Ni depletion in electrolysis mode, an integrated model is developed to investigate the effects of electrode microstructure evolution on cell performance, including both the Ni coarsening in electrolysis mode and the Ni depletion process. The PFM is mainly used to characterize the morphological changes due to electrode material migration, while the lattice Boltzmann method (LBM) based electrode model is used as a tool to quantify the electrochemical properties of electrodes. The above models have been validated by comparing preliminary simulation results with relevant experimental data. Using this integrated model, the evolution of important microstructural parameters of the electrode, such as the average particle size, TPB length (TPBl), under different degrees of Ni depletion is calculated. In addition, the effects of Ni depletion on the cell performance are also evaluated under different operating conditions is quantified and analyzed.

2. Model development

2.1 Phase-field model

The morphological evolution of the electrode during operation is captured by the phase-field model. Two sets of order parameters are used to describe the migration processes at the phase interfaces and grain boundaries. The conserved order parameters such as C_N, C_Y, and C_p represent the volume fractions of Ni, YSZ, and pore, respectively. Since the sum of the three is

1, only the volume fractions of Ni and YSZ need to be calculated. The non-conserved ordering parameters (η_1, η_2, …, $\eta_{m/n}$) are then used to indicate the grain orientations of the solid phases. For a point located in a solid phase with a defined crystal orientation k, the order parameters are specified as: $[C,\eta_1,\eta_2,...,\eta_k,...,\eta_{m/n}]=[1,0,0,...,\pm1,...,0]$. For the pore phase, these parameters are all zero. At the phase interface, the value of C changes smoothly from 0 to 1. Then the total system free energy (F_{total}) can be expressed as a function of the above parameters:

$$F_{total}=\int\left[f_0\left(\{C_i\},\{\eta_i\}\right)+\sum_i^m\frac{\kappa_i^N}{2}\left(\nabla\eta_i^N\right)^2+\sum_i^n\frac{\kappa_i^Y}{2}\left(\nabla\eta_i^Y\right)^2 +\sum_{i=N,Y}\sum_{j=N,Y}\frac{\kappa_C^{ij}}{2}\left(\nabla C_i\cdot\nabla C_j\right)\right]dv \tag{1}$$

where κ_i^N, κ_i^Y and κ_C^{ij} are the gradient energy coefficients. The first term in the integral represents the bulk free energy density. The second and third terms represent the residual interfacial energy at grain boundaries. The fourth term represents the residual interfacial energy at the phase interfaces. The bulk free energy density (f_0) can be expressed as:

$$f_0=\sum_{i=N,Y}\alpha_i f_1(C_i)+\alpha_{NY}f_1(C_N+C_Y)+\sum_{i=N,Y}\beta f_2(C_i)+\sum_i^m\delta f_3(C_N,\eta_i^m)+\sum_i^n\delta f_3(C_Y,\eta_i^n) +\sum_{i=1}^m\sum_{j\neq i}^m\varepsilon f_4\left(\eta_i^N,\eta_j^N\right)+\sum_{i=1}^n\sum_{j\neq i}^n\varepsilon f_4\left(\eta_i^Y,\eta_j^Y\right)+\gamma f_5\left(C_N,C_Y\right)+f_6(C_N,C_Y) \tag{2}$$

where

$$\begin{cases} f_1(C) = C^2(1-C)^2 \\ f_2(C) = \dfrac{1}{4}C^4 \\ f_3(C,\eta_i) = \dfrac{1}{2}C^2\eta_i^2 + \dfrac{1}{4}\eta_i^4 \\ f_4(\eta_i,\eta_j) = \dfrac{1}{2}\eta_i^2\eta_j^2 \\ f_5(C_N,C_Y) = \dfrac{1}{2}C_N^2C_Y^2 \\ f_6(C_N,C_Y) = -W_{ca}\left(C_N\left|\nabla C_Y\right|^2 + k\right) \end{cases} \tag{3}$$

Here, f_1 is a double-well potential function that depends on the volume fraction. f_2, f_3, f_4, and f_5 represent the coupling relation between different crystallographic orientations and volume fractions. f_6 indicates the energy density associated with the wettability of Ni on the YSZ surface, which is used to control the contact angle between Ni and YSZ and as a driving force for the migration of the Ni phase under gradient wettability. The value of W_{ca} is used to control the wettability and the contact angle [25]. Such values ensure that a determined point in the computational domain belongs to a phase with determined crystal orientation. The k in f_6 is a fixed value for all cases and is used as a regulation parameter for this chemical potential gradient to fit the Ni depletion experiment.

The mechanism of Ni migration is shown in Fig. 1 (b). In the present study, the hypothesis of Trini et al. [19] is adopted in the model. The local oxygen partial pressure can affect the wettability of Ni phase on the YSZ surface. Under the effects of negative polarization in SOEC mode, there will be a gradient of oxygen partial pressure in the direction perpendicular to the electrolyte with high negative polarization, which also leads to a gradient of wettability in this direction. The contact Angle between Ni and YSZ varies with the wettability. The region with

larger Ni wettability has a smaller contact angle and is characterized by smaller chemical potential. Then it is reasonable to assume that the driving force is the chemical energy gradient due to the change in wettability. It should be noted that the mechanism of Ni depletion during SOEC operation remains to be further confirmed. However, there is no corresponding experimental support for the contact angle corresponding to different adsorbed oxygen under the negative polarization effect of SOEC mode. Jiao et al. [26, 27] reported the enhancement of the wettability of Ni on the YSZ surface under the positive polarization of fuel cell mode and the weakening wettability under negative polarization of the electrolysis cell as well as the resulting changes in the Ni phase morphology. They found the surface adsorbed oxygen affects the surface tension of Ni, which in turn affects the wettability of Ni on the YSZ surface. This also provides the corresponding theoretical basis for the hypothesis of Trini et al [19]. A recent study showed that Ni enrichment was found during very long fuel cell operations (up to 10 years) [28]. This suggests that Ni migration may occur under positive polarization (fuel cell mode) in the opposite direction of negative polarization (electrolysis cell mode), which somehow proves the validity of the Ni migration mechanism hypothesis.

The decreasing trend of the total free energy is the driving force controlling the evolution of the electrode microstructure [29]. And this process is characterized as the changes of the order parameters over time. The volume fraction fields and grain orientation fields are controlled by the Cahn-Hilliard and Allen-Cahn equations, respectively:

$$\frac{\partial C_{\mathrm{i}}}{\partial t} = \nabla \cdot \left[M_{\mathrm{C}}^{\mathrm{i}} \nabla \left(\frac{\partial f_0}{\partial C_{\mathrm{i}}} - \sum_{\mathrm{j=N,Y}} \kappa_{\mathrm{C}}^{\mathrm{ij}} \nabla^2 C_{\mathrm{j}} \right) \right], \mathrm{i} = \mathrm{N}, \mathrm{Y} \tag{4}$$

$$\frac{\partial \eta_{\mathrm{i}}}{\partial t}=-L_{\mathrm{j}}\left(\frac{\partial f_0}{\partial \eta_{\mathrm{i}}}-\kappa \nabla^2 \eta_{\mathrm{i}}\right),\ \mathrm{i}=1,2,\ldots,\mathrm{m/n},\ \mathrm{j}=\mathrm{N/Y} \tag{5}$$

where M_c and L are the mobilities of phase fraction and grain orientations. In the calculation, the mobility for the YSZ phase is set as zero, and the ratio of grain boundary and phase gradient coefficients for the Ni phase is set to 0.71 [25]. The values of the relevant parameters in the above equations are listed in Table 1. In this study, a variable Ni mobility function is introduced to represent several different diffusion mechanisms of Ni coarsening, such as surface diffusion, volume diffusion and grain boundary diffusion. The conversion between dimensionless M_c, a function of conserved and non-conserved fields, and values of real mobilities can be found in our previous study [10].

Table. 1 Parameters in the PFM.

Parameters	Value
κ_C^{NN}, κ_C^{YY}, κ_C^{NY}	0.6, 0.6, 0.6
α_N, α_Y, α_{NY}	1.0, 0.2
β, δ, ε, γ, k	1, 1, 3, 1, 4
m, n	15, 15
L_N, L_Y	1.0, 1.0

2.2 Electrode model based on LBM

The heterostructure electrodes of SOCs have a more complex microscopic binding structure. This requires coupled multi-physics field simulations of complex real microstructures. The mesoscopic LBM has been shown to be a good method for modeling three-dimensional heterogeneous pore-scale transport phenomena [30]. Compared with macroscopic models, LBM can provide a more intuitive and accurate prediction of the transport processes inside electrodes. In this study, we performed coupled multi-physics field simulations of voxelized electrode microstructures derived from PFM based on LBM.

2.2.1 Mathematical model

The gas species transport is simulated by the dusty gas model. For a binary species system, only the transport of one gas component needs to be solved. By assuming the constant total pressure, the related transport equation can be expressed as [31]:

$$\nabla\left[\left(\frac{1\text{-}\alpha^{*} y_{\mathrm{H_2O}}}{D_{\mathrm{H_2,H_2O}}}+\frac{1}{D_{\mathrm{H_2O,k}}}\right)^{-1}\nabla C_{\mathrm{H_2O}}\right]=\frac{J}{2F} \tag{6}$$

where $\alpha^{*}=1\text{-}\left(M_{\mathrm{H_2O}}/M_{\mathrm{H_2}}\right)^{1/2}$, $C_{\mathrm{H_2}}$ (mol m^{-3}) is the species concentration, J (A m^{-3}) is the electrochemical reaction rate, F (C mol^{-1}) is the Faraday constant, $M_{\mathrm{H_2}}$ and $M_{\mathrm{H_2O}}$ (kg mol^{-1}) is the average molar mass.

The Knudsen diffusion coefficient and the binary diffusion coefficient can be calculated as [32]:

$$D_{\mathrm{i,k}}=\frac{d_{\mathrm{p}}}{3}\sqrt{\frac{8RT}{\pi M_{\mathrm{i}}}} \tag{7}$$

$$D_{i,j}=\frac{0.0101T^{1.75}}{p\left(\frac{2M_iM_j}{M_i+M_j}\right)^{1/2}\left[V_i^{1/3}+V_j^{1/3}\right]^2} \tag{8}$$

where d_p (μm) is the average pore diameter, V_i (cm^{-3} mol^{-1}) is the special Fuller diffusion volume.

The Ni and YSZ phases act as the conductors of electrons and ions, respectively. The related conservation equations can be expressed as [33]:

$$0=\nabla\cdot\left(\sigma_{ele}\nabla\phi_{ele}\right)-J \tag{9}$$

$$0=\nabla\cdot\left(\sigma_{ion}\nabla\phi_{ion}\right)+J \tag{10}$$

where σ_{ele} and σ_{ion} (S m^{-1}) are the conductivities. φ_{ele} and φ_{ion} (V) are the electronic and ionic potentials, respectively.

The electrochemical reaction rate is calculated by the Butler-Volmer equation:

$$J=j_0\left(\exp\left(\alpha_e\frac{n_eF}{RT}\eta_{act}\right)-\exp\left(-\left(1-\alpha_e\right)\frac{n_eF}{RT}\eta_{act}\right)\right) \tag{11}$$

where α_e, n_e are the charge transfer coefficient and the number of electrons transferred per reaction, respectively. The activation overpotential (η_{act}) is calculated as: $\eta_{act}=\varphi_{ion}-\varphi_{ele}$. The exchange current density j_0 (A m^{-3}) is defined as [33]:

$$j_0=\gamma_a\frac{L_{TPB}}{\lambda_{TPB}}\left(\frac{p_{H_2O}}{p_{ref,H_2O}}\right)^q\exp\left(-\frac{E_{act,H_2O}}{RT}\right) \tag{12}$$

where γ_a is the adjustable parameter to fit the experimental data. L_{TPB} (μm μm^{-3}) is the local TPB density, and λ_{TPB} is the parameter that relates the real TPB density and the stair-step shape of TPB segments. Here, the value of λ_{TPB} is set as 1.455 [34]. p_{H_2O} and p_{ref,H_2O} (Pa) are the partial pressure and reference pressure of H_2O, respectively. E_{act,H_2O} (J mol^{-1}) is the activation

energy. The values of related electrochemical parameters are listed in Table 2.

Table. 2 Electrochemical parameters and operating conditions.

Parameters	Value
Electrochemical parameters	
Charge transfer coefficient, α_e	0.5
Number of electrons transferred per reaction, n_e	2.0
Adjustable parameter, γ_a	2.0×10^5
Reference pressure, p_{ref,H_2O} (Pa)	101,325
Activation energy, E_{act,H_2O} (J mol^{-1}) [32]	120,000
Exponent for exchange current density, q	0.5
Electric conductivity of electron conductor, σ_{ele} (S m^{-1}) [30]	$\frac{4.2\times10^7}{T}\exp\left(\frac{-1200}{T}\right)$
Electric conductivity of ion conductor, σ_{ion} (S m^{-1}) [30]	$33.4\times10^3\exp\left(\frac{-10300}{T}\right)$
Operating conditions at base case	
Operating pressure (atm)	1
Operating current density (A m^{-2})	12000
Operating temperature (K)	1123
Gas composition	50% H_2, 50% H_2O

2.2.2 Lattice Boltzmann method

The lattice Boltzmann method with the multiple-relaxation-time (MRT) collision operator is used in this study to describe the coupled multi-physics process. Compared to the other schemes, the MRT can offer higher numerical stability [35]. Meanwhile, the D3Q7 lattice scheme is adopted, which can improve the computational efficiency without any loss of accuracy. The evolution of LBM equation with MRT operator can be expressed as:

$$f_{\mathrm{i}}\left(\boldsymbol{x}+\boldsymbol{e}_{\mathrm{i}}\Delta t, t+\Delta t\right)-f_{\mathrm{i}}(\boldsymbol{x},t)=-\boldsymbol{M}^{-1}\boldsymbol{\Lambda}\boldsymbol{M}\left(f_{\mathrm{i}}\left(\boldsymbol{x},t\right)-f_{\mathrm{i}}^{\mathrm{eq}}\left(\boldsymbol{x},t\right)\right) \tag{13}$$

where f_{i} is the density distribution function in the ith direction. The discrete velocity $\boldsymbol{e}_{\mathrm{i}}$ can be given as:

$$\boldsymbol{e}_{\mathrm{i}}=\begin{cases}(0,0,0) & \mathrm{i}=0\\ (\pm c,0,0),(0,\pm c,0),(0,0,\pm c) & \mathrm{i}=1-6\end{cases} \tag{14}$$

The lattice sound speed $c = \Delta x/\Delta t$, where Δx and Δt are the lattice space and the time step, respectively. $\boldsymbol{M}$ and $\boldsymbol{\Lambda}$ are the transformation matrix and the corresponding diagonal relaxation matrix, respectively, given as:

$$\boldsymbol{M}=\begin{pmatrix}1 & 1 & 1 & 1 & 1 & 1 & 1\\ 0 & 1 & -1 & 0 & 0 & 0 & 0\\ 0 & 0 & 0 & 1 & -1 & 0 & 0\\ 0 & 0 & 0 & 0 & 0 & 1 & -1\\ 6 & -1 & -1 & -1 & -1 & -1 & -1\\ 0 & 2 & 2 & -1 & -1 & -1 & -1\\ 0 & 0 & 0 & 1 & 1 & -1 & -1\end{pmatrix} \tag{15}$$

$$\boldsymbol{\Lambda}=diag\left(\tau_0^{-1}\ \tau_1^{-1}\ \tau_2^{-1}\ \tau_3^{-1}\ \tau_4^{-1}\ \tau_5^{-1}\ \tau_6^{-1}\right) \tag{16}$$

The equilibrium distribution function can be given by: $f_{\mathrm{i}}^{\mathrm{eq}}\left(\boldsymbol{x},t\right)=\omega_{\mathrm{i}}C$ with C calculated as $C=\sum_{\mathrm{i}=0}^{6} f_{\mathrm{i}}\left(\boldsymbol{x},t\right)$. The weight coefficients ω_{i} are given as: $\omega_0 = k_0$, $\omega_{1\text{-}6} = (1\text{-}k_0)/6$. The isotropic

diffusion is adopted in this study, and the relaxation coefficients τ_i are given as:

$$\begin{cases} \tau_0 = 1 \\ \tau_{1-3} = \dfrac{1}{2} + \dfrac{1}{c\Delta x\left(1-k_0\right)/3} D \\ \tau_{4-6} = \dfrac{1}{2} + \dfrac{1}{6\left(\tau_{1-3} - 1/2\right)} \end{cases} \tag{17}$$

The diffusivity of H_2O transport (D_{H_2O}) is usually several orders of magnitude lower than that of ions, which will lead to a large difference in the relaxation coefficients. This is also true for ions compared to electrons. In order to avoid the resulting numerical instability, an artificial diffusivity of D_0 is adopted with the same order of magnitude as D_{H_2O} for the electrons and ions transport calculations [36]. This treatment can guarantee the numerical robustness of the coupling between ion/electron and gas phase transport processes. By adopting the artificial diffusivity, the conservation equation of ion and electron can be formed as:

$$0 = \nabla \cdot \left(D_0 \nabla \phi_{\text{ion/ele}} \right) \pm D_0 J / \sigma_{\text{ion/ele}} \tag{18}$$

2.3 Numerical procedure

Both the PFM and the electrode model based on LBM are implemented by compiling in-house code with the CUDA C language based on GPU parallel acceleration. The equations. (4) and (5) in the PFM are solved by the semi-implicit Fourier-spectral method [37]. It can provide better partial accuracy while employing larger time steps compared to the finite difference method. In this study, the dimensionless time step is set as 0.05. The whole simulation process is as follows: firstly, the volume fraction field obtained by a sintered particle-packing structure

is used as the initial field of the PFM (the corresponding parameters are shown in Table. 1). Then the PFM is used to simulate the microstructure evolution. The size of the computational domain is 20×20×20 μm^3 with a discrete voxel field of 256×256×256. It should be mentioned that a field of size 10×10×15 μm^3 is intercepted as the computational domain for quantifying microstructural parameters and performing electrochemical calculations. Considering the length of the severe Ni depletion region (about 4 μm), this computational domain ensures good computational efficiency with a good characterization of Ni depletion effects. The domain side length in LBM calculation is around 12.5 times larger than the mean particle diameter, which is large enough to eliminate the randomness of microstructure generation. The characteristic length (l_0) is about 78 nm, which is around 1/10 of the mean particle diameter, indicating that the grid size is small enough to characterize the microstructure [38,39]. And the characteristic time (t_0) in the calculation of PFM is 1 h.

The voxelized fields derived from the PFM are used as input to quantify the relevant microstructure parameters as well as the computational domain of the electrode model. Thus, the evolution of microstructure and electrochemical performance can be quantified and analyzed. Part of the electrolyte is added to the bottom of the computational domain with the size of 10 grids (~0.78 μm). The top surface is identified as the interface of the active layer and the support layer. For the boundary conditions of the electrode model, the Neumann boundary conditions with constant current flux are applied at the bottom and top surface of the domain to describe the ion and electron transports, respectively. The thick support layer can cause significant mass transport resistance. However, the support layer is not included in the

computational domain, so the corresponding gas composition, i.e., the Dirichlet boundary, is specified on the surface of the computational domain. And the schematic of computational domain and boundary conditions is shown Fig. 1(c).

2.4 Model validation

2.4.1 Contact angle of Ni on YSZ surface

The contact angle of the Ni phase on the YSZ surface in this study is controlled by the wettability coefficient W_{ca}. The systems with a larger value of W_{ca} have smaller interfacial energy, which means that the Ni phase tends to expand more on the YSZ surface, forming a smaller contact angle. The contact angles corresponding to the different values of W_{ca} are shown in Fig. 2(a). According to the above, the chemical potential gradient caused by the wettability change is assumed to be the driving force of Ni phase migration. The wettability change is due to the change of contact angle caused by the Ni surface adsorbed oxygen under polarization. It should be emphasized that the study of Ni-YSZ contact angle at different humidity and negative polarization in SOEC mode is very helpful to elucidate the Ni depletion mechanism and will be a great guide for future simulation work. In this work, for simplicity, three minimum values of W_{ca} (0, 2, 3) are selected to represent three different degrees of Ni depletion at severe, moderate, and low levels, respectively. For the non-depletion cases, the value of W_{ca} is 4 to highlight the driving force of chemical potential gradient in the whole domain. For the depletion cases, the value of W_{ca} gradually increases linearly to 4 as the

distance from electrolyte increases.

2.4.2 Validation on morphology evolution and electrode model

Fig. 2(b)-(e) shows the comparisons between the experimental data and the simulation results. Firstly, for the non-depletion cases, i.e. fuel cell mode or open-circuit electrolysis cell mode, the evolutions of the average particle diameter and TPBl density shown in Fig. 2(b) and (c) are fitted with the experiment data [6]. The difference between the Ni volume fraction and the initial value in the direction perpendicular to the electrolyte is used as a control parameter to quantify the effects of Ni depletion, and the comparison is shown in Fig. 2(d). This figure is obtained by calculating the difference in Ni volume fraction at the same position between the reference electrode (no depletion) and the Ni-depletion electrode. And the severe Ni depletion case is used for the comparison. In this study, the initial microstructure of the Ni migration process is the two-phase particle-packing structure after a sintering process. Then, this initial microstructure is used in the phase-field calculation process. The initial microstructural parameters in the simulations are consistent with the experimental data [21] as much as possible, and the relevant parameters are compared in Table 3. The overall trends of two curves are generally consistent. After a long operation time (~10,000 h), compared to the initial state, the Ni volume fraction of the fuel electrode is decreased near the fuel electrode- electrolyte interface. Meanwhile, there is slight increase in Ni volume fraction away from the fuel electrode-electrolyte interface. By equating the rest of the single cell to resistance, the

polarization curves can be obtained. As shown in Fig. 2(e), the polarization curves calculated by the model fit well with the experimental data [21]. In addition, as shown in Fig. 2(f), the morphological comparison of experimental and simulation results is performed. The simulated time is similar to the experimental cell operating time of about 10,000 h. The image on the left shows the electrode cross-sections obtained from scanning electron microscopy and energy dispersive X-ray spectroscopy tests [16], with the Ni phase in red. The right image shows the cross-section of the simulation results of this study, with the Ni phase in white. It can be seen that the Ni phase distributions in the two figures match morphologically.

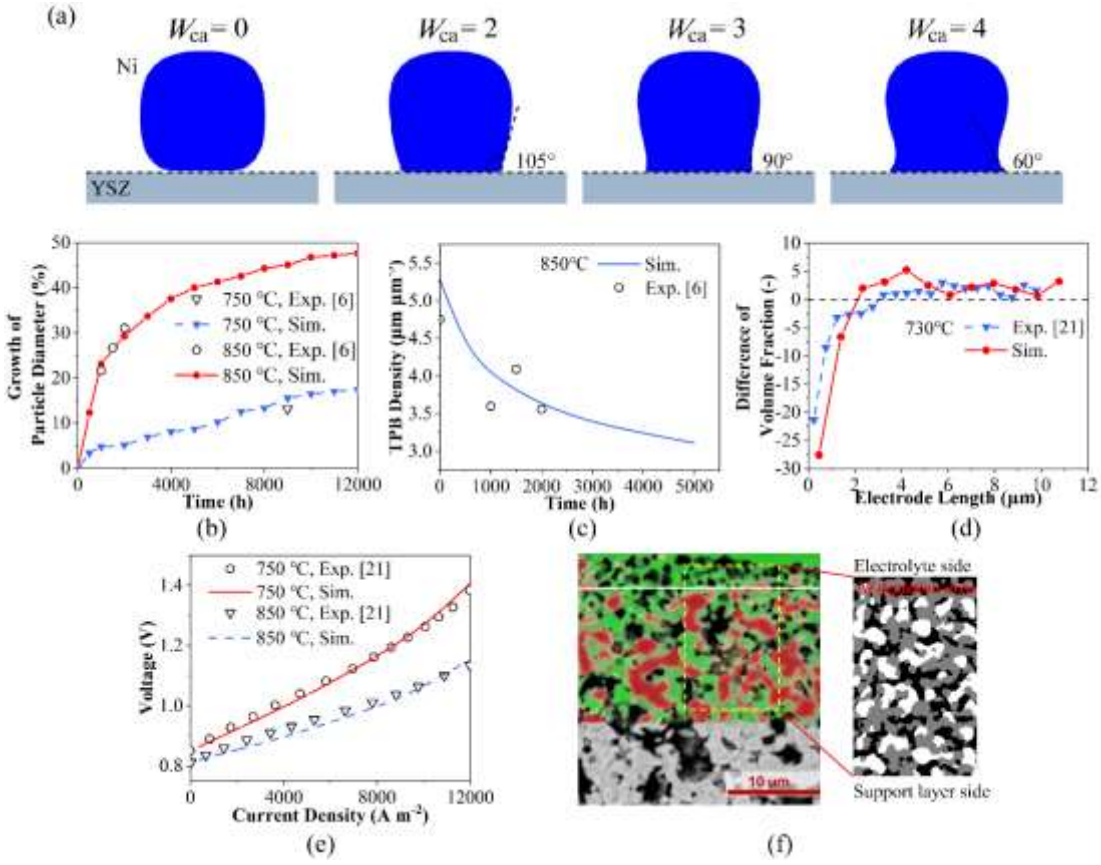

Fig. 2. (a) Contact angles of Ni on YSZ surface with different W_{ca}. The comparison between experimental data and simulation results on (b) Ni particle diameter, (c) density of TPB, (d)

difference of Ni volume fraction, and (e) polarization curves. The morphological comparison between cross-sections obtained from experiment [16] and simulation. left: Ni in red and YSZ in green, and right: Ni in white and YSZ in grey.

Table. 3 Comparison between initial microstructures.

Parameters	porosity	Ni volume fraction	TPBl (μm $μm^{-3}$)	Interfacial area ($μm^2$ $μm^{-3}$)	Average particle diameter (μm)
Validation case	28.3	30.8	5.28	1.97	0.68
Experiment data [21]	29	28.7	6.03	1.71	0.46

3. Results and discussion

3.1 Morphology analysis

The evolution of fuel electrodes is mainly due to the Ni coarsening and depletion phenomena. The Ni coarsening occurs in both operating modes as well as in the states of open circuit and polarization. As mentioned above, Ni depletion is due to the interaction and common effects of various factors [15], such as inlet gas humidity, operating current, etc. This study focuses on

the morphology evolution of the electrode under different levels of Ni depletion and the resulting electrochemical performance degradation. And the values of W_{ca} are used to characterize the degree of Ni depletion according to the Ni migration mechanism.

Fig. 3 shows the microstructure of the fuel electrode and the comparison of TPB distribution for different Ni depletion cases with 5000 h operation time. In Fig. 3(a), the bottom surface is the interface between the active layer and the electrolyte. Compared with the initial form, the Ni phases are all coarsened to some extent. The TPB network also becomes sparse. The severe Ni depletion creates the porous YSZ layer due to the migration of the Ni phase. In the experimental cross-sectional view of Fig. 2(f), there are some isolated Ni particles in the Ni depletion area, while such isolated particles are rarely present in the simulation. This is mainly because in practice some of the isolated Ni particles close to the electrolyte are not subjected to the same strong negative polarization as the rest of the percolated Ni particles, which results in the absence of a longitudinal migration drive force. Due to the difficulty in considering the Ni particles percolation in PFM, all Ni particles are assigned to the migration drive force for simplicity, but this has a negligible effect on the relevant morphological and electrochemical analysis, since any isolated Ni particles do not contribute to effective TPB. As shown in Fig. 3(b), the evolution of the TPB network shows a decrease in the effective TPB distribution area with the increase of Ni depletion on the one hand, and a decrease in TPB density to some extent on the other hand. Different depletion levels also affect the Ni coarsening rate, which is responsible for the decrease in TPB density. The active TPBl density decreases from 5.18 $\mu m \cdot \mu m^{-3}$ of the initial state to 1.94 $\mu m \cdot \mu m^{-3}$ of the severe depletion case. Meanwhile, the

evolution of the electrode morphology is the result of the combined effect of various microstructural parameters, such as particle size, porosity, volume fraction, and surface area. For example, smaller particle size leads to faster Ni coarsening, and excessive volume fraction of Ni or YSZ leads to insufficient percolation rate, resulting in small active TPBl density.

In addition, the morphology evolution may cause impacts on the thermal mechanical properties of electrode. Generally speaking, the main cause of microcracks inside electrodes and delamination between electrode and electrolyte is the mismatch of thermal expansion coefficients (TEC) between materials and between different layers. However, there is still a gap in research related to the influence of electrode evolution such as Ni phase migration on thermomechanical properties. Especially for SOEC, the changes of electrode thermomechanical properties under severe Ni depletion need to be further investigated.

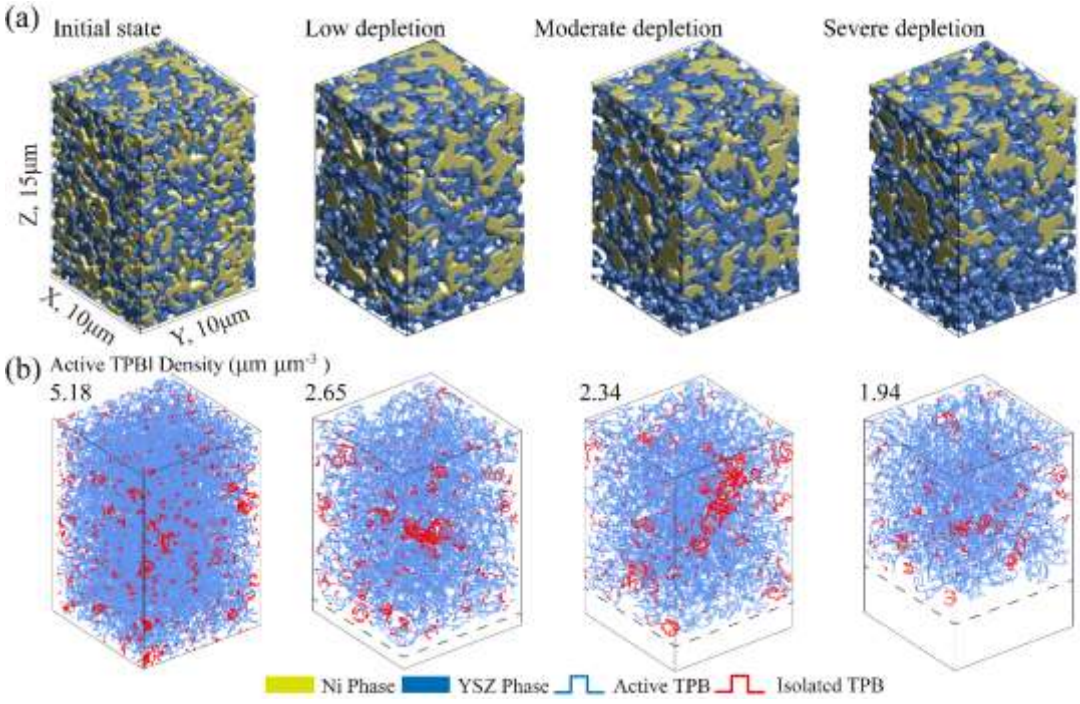

Fig. 3. Effects of Ni depletion on the morphology of fuel electrode: (a) Ni-YSZ composite; (b) TPB network.

Fig. 4 shows the evolution of particle size, TPB density, and width of depletion region over time for different depletion levels. For the non-depletion case, the average Ni particle size increases from 0.812 μm to 1.077 μm, and the TPB density decreases from 5.759 $\mu m \cdot \mu m^{-3}$ to 3.154 $\mu m \cdot \mu m^{-3}$ after 5000 h. For the severe Ni depletion, the average Ni particle size increases to 1.166 μm, while the TPB density decreases to 2.076 $\mu m \cdot \mu m^{-3}$. It can be seen that the magnitude of the variation of Ni particle size, as well as TPB density, enhances with increasing depletion at the same coarsening mobility. Fig. 4(c) shows the evolution of the depletion region width over time. Here the depletion region width (W_{depl}) is defined as the product of the number of layers with longitudinal Ni phase volume fraction less than 0.01 and the characteristic length.

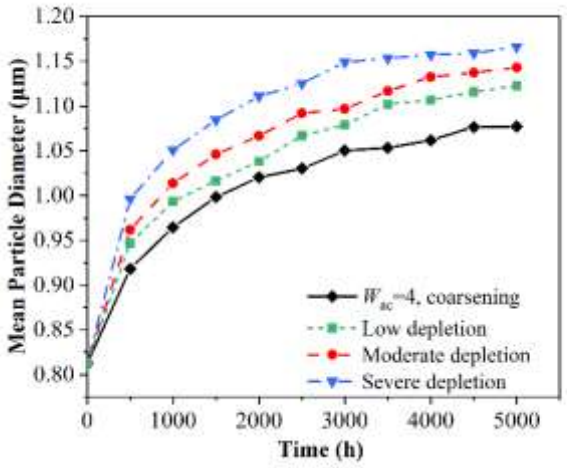

(a)

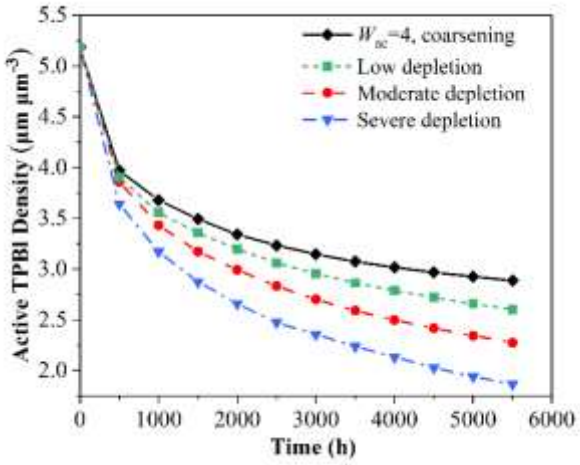

(b)

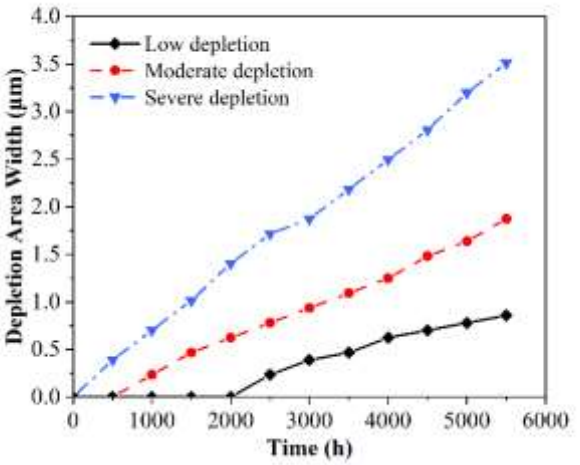

(c)

Fig. 4. The changes of microstructural parameters over time: (a) average Ni particle diameter, (b) Active TPBl density, and (c) depletion area width.

In addition, the effects of wettability on the morphology evolution are shown in Fig. 5. It can be seen that the Ni coarsening decreases with increasing wettability (Fig. 5 (a)). In particular, at a contact angle of 30° (W_{ca}=5), the average Ni particle size only increases by 19.5% after

5000 h. The larger wettability has a certain inhibitory effect on Ni coarsening. Fig. 5(b) shows the evolution of TPBl density over time with different wettabilities. It should be noted that the difference in TPBl density reduction is small except for the case of a smaller contact angle (W_{ca} =5). This is related to the Ni-YSZ interfacial area, and the corresponding interfacial areas are listed in Table 4. The evolution of interfacial areas mainly occurs in the first 1000 h. For the small contact angle case, the interfacial area increases compared to the initial value. For other cases, the stabilized interface area is smaller compared to the initial value. Some studies have found that the use of Ni alloys doped with other substances results in a certain degree of expansion of the three interface areas [40,41]. Increasing wettability is achieved by reducing the interfacial energy. Overall there are several strategies to enhance the wettability. As mentioned above, the first is to dope some other substances in the Ni phase. Secondly, the stability of Ni on YSZ surface can be improved by adjusting the operating conditions of the solid oxide cell and reducing the polarization and humidity [15]. In addition to this, epitaxial bonding between YSZ and Ni particles can be created electrochemically to reduce the interfacial energy [42]. Thus, increasing the wettability of the Ni phase in the YSZ surface can effectively suppress the reduction of TPB density due to Ni coarsening. For the binary Ni-YSZ system with a larger wettability, the Ni particles tend to extend towards the YSZ surface during the evolution process. In this way, the agglomeration of small Ni particles is hindered to a certain extent and the Ni coarsening is inhibited.

Table. 4 Ni-YSZ interfacial areas of initial and degraded cases.

	Initial	W_{ca}=2	W_{ca}=3	W_{ca}=4	W_{ca}=5
Interfacial area ($\mu m^2\ \mu m^{-3}$)	1.59	1.28	1.4	1.53	1.69

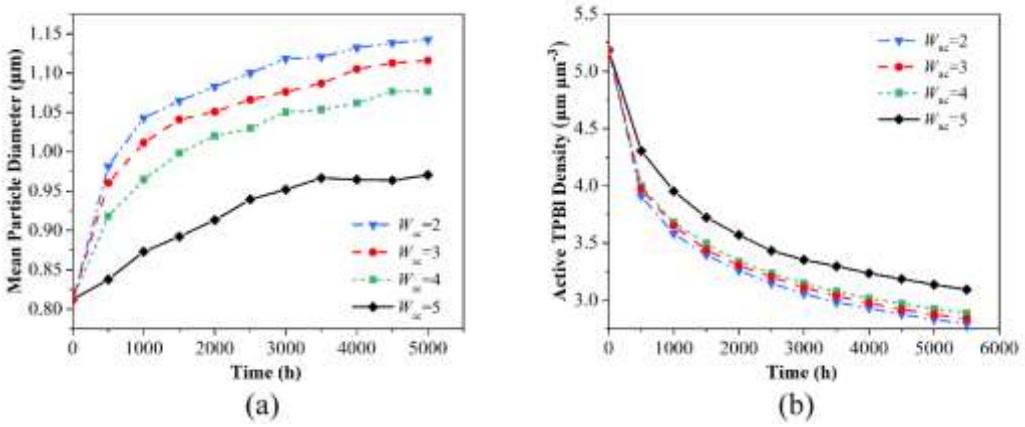

Fig. 5. Effects of wettability on the morphology evolution.

3.2 Electrochemistry analysis

Fig. 6 shows the overpotential-current density curves with different levels of depletion. In the cases of 850℃, at high current density (12,000 A m^{-2}), the total overpotential increases by 52.8% (0.081 V, from 0.153 to 0.234 V) compared to non-depletion case, with the activation overpotential increasing by 0.03 V (from 0.069 to 0.099 V) and the ohmic overpotential increasing by 0.051 V (from 0.084 to 0.135 V). We attribute the increase in activation overpotential mainly to the decrease in TPBl. However, whether there are other factors

contributing to the increase needs to be experimentally verified in the future. In addition, the increase of ohmic overpotential is another major cause of electrochemical degradation of the electrode. Some previous experimental studies have also observed that Ni depletion leads to a large increase in ohmic resistance [14,21,43]. For conventional Ni-YSZ electrodes, the ohmic overpotential is mainly caused by the YSZ phase due to its low ionic conductivity compared to the Ni phase. By comparing the polarization curves between the initial case and the non-depletion case, we can see that the variation of ohmic loss is small. The total overpotential increases by 0.037 V (from 0.116 to 0.153 V) at 12,000 A m^{-2}. This means that Ni coarsening mainly increases the activation overpotential. In the cases of 800°C, the overall trend remains the same. But all values of overpotential are greatly increased.

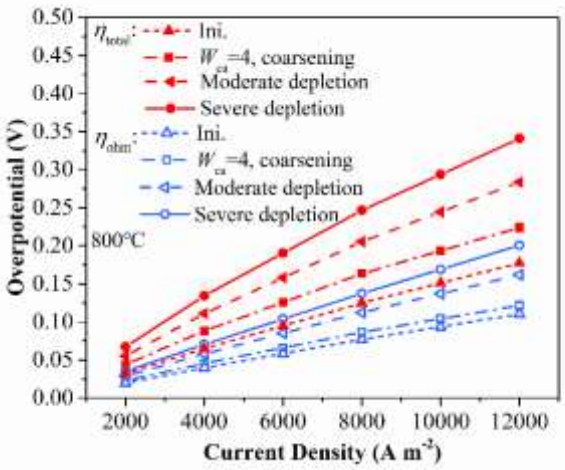

(a)

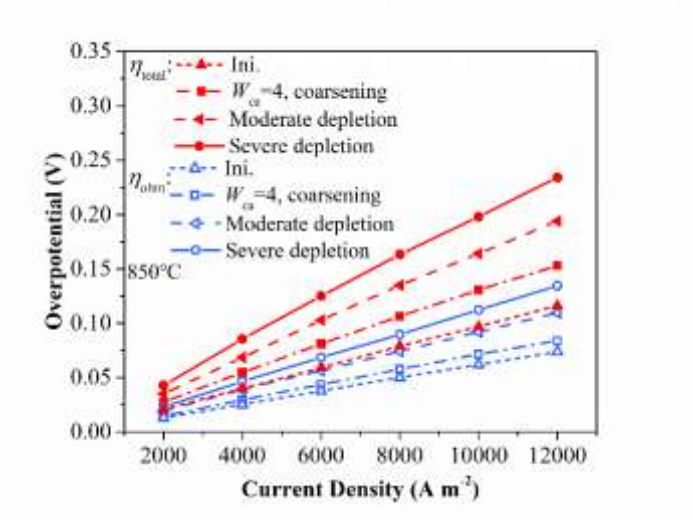

(b)

Fig. 6. The overpotential-current density curves with different degrees of Ni depletion.

Fig. 7 illustrates the distribution of the ionic potential, and the dashed line marks the intersection of the effective reaction layer with the porous YSZ layer produced by Ni depletion. It can be seen that the difference of ion potential distribution in the xy-axis cross-section is very small, and the absolute value of potential decreases gradually from the electrolyte side along the direction perpendicular to the electrolyte layer. The potential difference between the two end surfaces is the ionic potential loss. Under severe depletion condition, the ionic potentials on both sides of the porous YSZ layer have a large difference, which indicates that a large ionic potential loss is generated in this region. Meanwhile, the ionic potential loss of the severe depletion case is significantly greater than that of other cases. On the one hand, since severe depletion leads to a significant increase of the porous YSZ layer thickness, this results in an increase of the local ionic current within this layer under the same operating current density.

This increases the ohmic loss in the effective active layer. On the other hand, for the non-depletion electrode, the electrochemical reaction is concentrated near the dense electrolyte (at the electrode-electrolyte interface). Ni depletion directly leads to the fact that oxygen ions generated by electrochemical reactions have to pass through an extra porous YSZ layer to reach the dense electrolyte and then be transported to the oxygen electrode to participate in the reaction. That is, the presence of a porous YSZ layer directly extends the ion transport path between the effective reaction sites and the dense electrolyte, leading to higher ohmic loss.

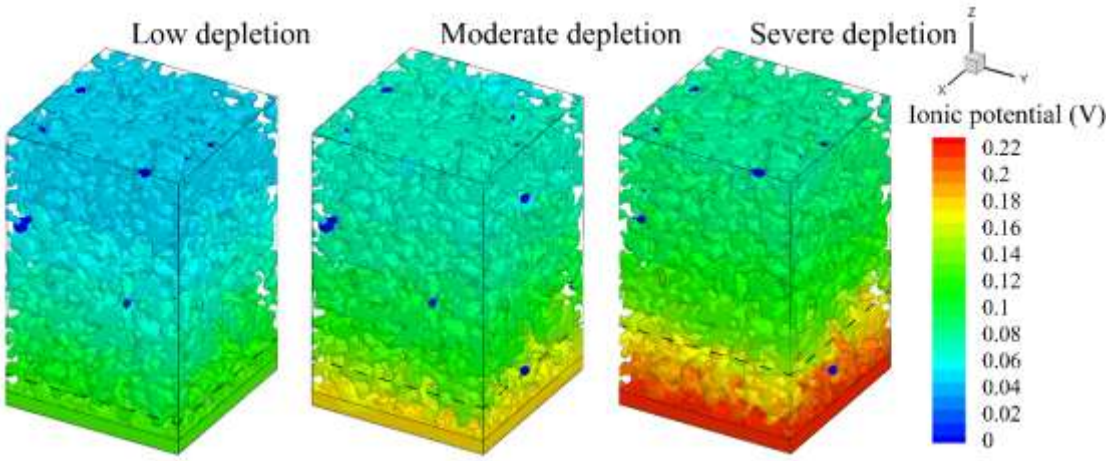

Fig. 7. The ionic potential distributions with different degrees of Ni depletion.

Fig. 8 (a) and (b) illustrates the distribution of the activation overpotential in the direction of electrode thickness. As shown in Fig. 8 (a), the severe depletion raises the average activation overpotential from 0.069 V to 0.099 V. This is mainly due to the reduction of the effective reaction sites caused by Ni depletion. The dashed lines mark the depletion region width, in which no electrochemical reaction occurs due to the absence of effective reaction sites. The

effects of operating current density are also shown in Fig. 8 (b). Compared to the low current density case, the reaction at high current density is concentrated near the electrolyte layer, so there is a high gradient of overpotential here. Fig. 8 (c) and (d) shows the average electrochemical reaction rate distribution along the direction perpendicular to the electrolyte for different influencing factors. As shown in Fig. 8 (c), for non-depletion case, the electrochemical reactions are mainly concentrated near the electrolyte. With the increase of Ni depletion and the migration of reaction sites, the electrochemical reaction is shifted away from this interface. For the Ni depletion case, there is a rapid increase in the reaction sites at the interface of the Ni depletion region and the main reaction region. Moreover, the overall electrochemical reaction rate is significantly higher in the non-depletion region than in the non-depletion case. This is mainly due to the increase of the active TPBl density brought about by Ni migration in the non-depleted region. In addition, the distribution of the electrochemical reaction rates at different operating currents is shown in Fig. 8 (d). For low current density case, the electrochemical reaction is more uniform. However, for high current case, the electrochemical reaction rates on both sides of the electrode differ significantly. The reactions at high operating currents are more concentrated near the electrolyte layer.

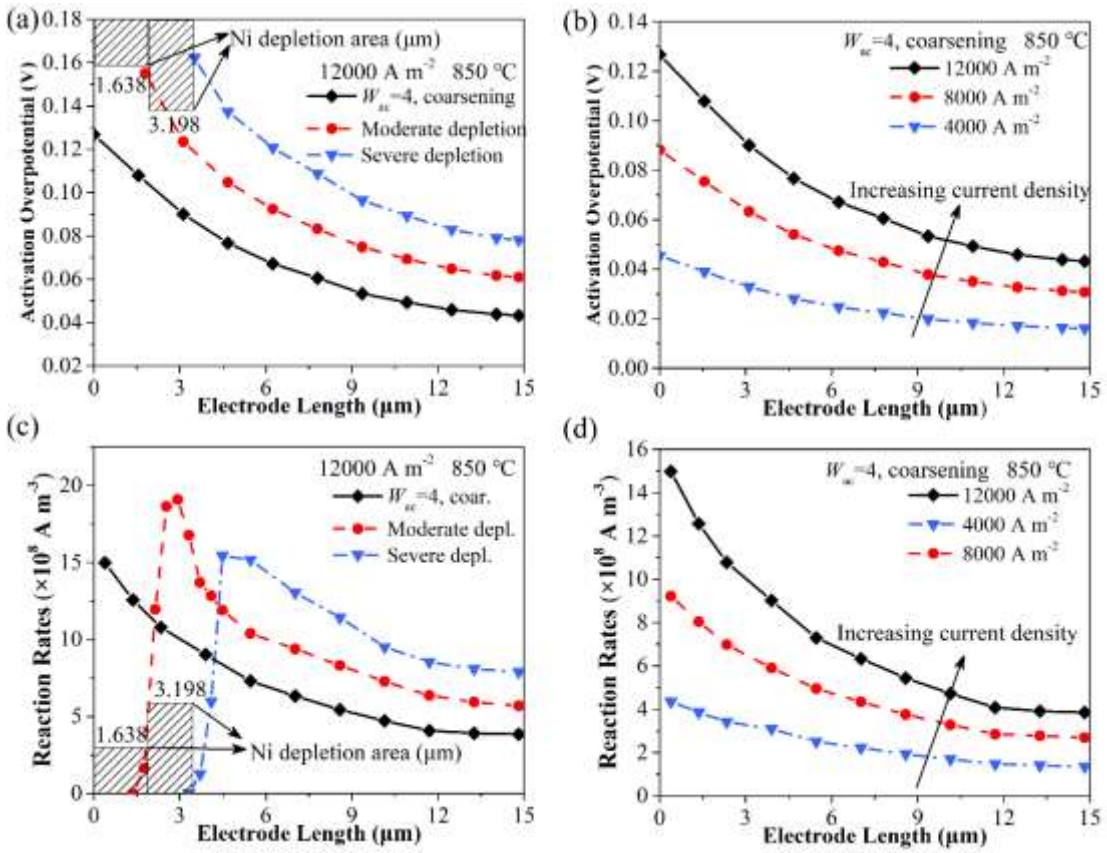

Fig. 8. The distribution of (a)(b) activation overpotential and (c)(d) electrochemical reaction rates in the direction of electrode thickness: (a) and (c) effects of depletion; (b) and (d) effects of working current density.

4. Conclusions

In this study, an integrated model is developed to study the fuel electrode degradation due to microstructure changes during SOEC operation. The electrode microstructure evolution of SOEC fuel electrodes mainly includes Ni coarsening and Ni depletion, and the phase-field model is used to characterize the change of electrode morphology during these processes. In addition, the resulting electrochemical performance degradation is evaluated with an LBM-

based electrode model. The microstructural parameters and the electrochemical performance during the evolution of the electrode are fitted experimentally and the results are in good agreement. In terms of morphology, Ni depletion has the greatest impact on electrode degradation. This phenomenon causes the Ni phase to migrate away from the electrode-electrolyte interface towards the surface of the electrode surface, resulting in the appearance of a porous YSZ layer, with depletion region width up to several microns in severe cases. Ni coarsening and TPBl density reduction also increase with increasing Ni depletion. For non-depletion cases, increasing the wettability of Ni on the YSZ surface can suppress Ni coarsening and maintain the TPBl density to a certain extent. In terms of electrochemical performance, severe Ni depletion increases the overall overpotential of the cell by 52.8% under basic case. The Ni depletion region increases the oxygen ion transport path and thus increases the ohmic resistance. With the increase of Ni depletion, the electrochemical reaction area will expand away from the electrode-electrolyte interface. The integrated model developed in this study can be used to quantify the irreversible performance loss caused by Ni migration during SOEC operation. Meanwhile, more work on Ni migration inhibition is needed in the future to improve the overall durability of SOEC.

Code availability

The codes used in this study are available from the corresponding author upon reasonable request.

Acknowledgement

This work is supported by the National Key Research and Development Program of China (2017YFB0601904). M. NI also thanks the grants (Project Number: PolyU 152064/18E and N_PolyU552/20) from Research Grant Council, University Grants Committee, Hong Kong SAR.

References

[1] Sinsel SR, Riemke RL, Hoffmann VH. Challenges and solution technologies for the integration of variable renewable energy sources—a review. Renewable Energy 2020; 145: 2271-2285.

[2] Østergaard PA, Duic N, Noorollahi Y, Mikulcic H, Kalogirou S. Sustainable development using renewable energy technology. Renewable Energy 2020; 146: 2430-2437.

[3] Mohammadi A, Mehrpooya M. A comprehensive review on coupling different types of electrolyzer to renewable energy sources. Energy 2018; 158: 632-655.

[4] Zheng Y, Wang J, Yu B, Zhang W, Chen J, Qiao J, Zhang J. A review of high temperature co-electrolysis of H_2O and CO_2 to produce sustainable fuels using solid oxide electrolysis cells (SOECs): advanced materials and technology. Chemical Society Reviews 2017; 46: 1427-1463.

[5] Hauch A, Küngas R, Blennow P, Hansen AB, Hansen JB, Mathiesen BV, Mogensen MB.

Recent advances in solid oxide cell technology for electrolysis. Science 2020; 370: 6513.

[6] Hubert M, Laurencin J, Cloetens P, Morel B, Montinaro D, Lefebvre-Joud F. Impact of Nickel agglomeration on Solid Oxide Cell operated in fuel cell and electrolysis modes. Journal of Power Sources 2018; 397: 240-251.

[7] Moçoteguy P, Brisse A. A review and comprehensive analysis of degradation mechanisms of solid oxide electrolysis cells. International Journal of Hydrogen Energy 2013; 38.36: 15887-15902.

[8] Khan MS, Lee SB, Song RH, Lee JW, Lim TH, Park SJ. Fundamental mechanisms involved in the degradation of nickel–yttria stabilized zirconia (Ni–YSZ) anode during solid oxide fuel cells operation: a review. Ceramics International 2016; 42: 35-48.

[9] Wang Y, Li W, Ma L, Li W, Liu X. Degradation of solid oxide electrolysis cells: Phenomena, mechanisms, and emerging mitigation strategies—A review. Journal of Materials Science & Technology 2020; 55: 35-55.

[10] Wang Y, Wu C, Du Q, Ni M, Jiao K, Zu B. Morphology and performance evolution of anode microstructure in solid oxide fuel cell: A model-based quantitative analysis. Applications in Energy and Combustion Science 2021; 5: 100016.

[11] De Angelis S, Jørgensen PS, Tsai EHR, Holler M, Kreka K, Bowen JR. Three dimensional characterization of nickel coarsening in solid oxide cells via ex-situ ptychographic nano-tomography. Journal of Power Sources 2018; 383: 72-79.

[12] Zekri, A., Herbrig K, Knipper M, Parisi J, Plaggenborg T. Nickel Depletion and Agglomeration in SOFC Anodes During Long-Term Operation. Fuel Cells 2017; 17.3:

359-366.

[13] Trini M, Jørgensen PS, Hauch A, Bentzen JJ, Hendriksen PV, Chen M. 3D microstructural characterization of Ni/YSZ electrodes exposed to 1 year of electrolysis testing. Journal of The Electrochemical Society 2019; 166: F158.

[14] Rinaldi G, Diethelm S, Oveisi E, Burdet P, Van Herle J, Montinaro D, et al. Post-test analysis on a solid oxide cell stack operated for 10,700 hours in steam electrolysis mode. Fuel Cells 2017; 17: 541-549.

[15] Hoerlein MP, Riegraf M, Costa R, Schiller G, Friedrich KA. A parameter study of solid oxide electrolysis cell degradation: Microstructural changes of the fuel electrode. Electrochimica Acta 2018; 276: 162-175.

[16] Frey CE, Fang Q, Sebold D, Blum L, Menzler NH. A detailed post mortem analysis of solid oxide electrolyzer cells after long-term stack operation. Journal of The Electrochemical Society 2018; 165: F357.

[17] Schäfer D, Fang Q, Blum L, Stolten D. Syngas production performance and degradation analysis of a solid oxide electrolyzer stack. Journal of Power Sources 2019; 433: 126666.

[18] Mogensen MB, Hauch A, Sun X, Chen M, Tao Y, Ebbesen SD, et al. Relation between Ni particle shape change and Ni migration in Ni–YSZ electrodes–a hypothesis. Fuel cells 2017; 17: 434-441.

[19] Trini M, Hauch A, De Angelis S, Tong X, Hendriksen PV, Chen M. Comparison of microstructural evolution of fuel electrodes in solid oxide fuel cells and electrolysis cells. Journal of Power Sources 2020; 450: 227599.

[20] Hauch A, Brodersen K, Chen M, Mogensen MB. Ni/YSZ electrodes structures optimized for increased electrolysis performance and durability. Solid State Ionics 2016; 293: 27-36.

[21] Monaco F, Hubert M, Vulliet J, Ouweltjes JP, Montinaro D, Cloetens P, et al. Degradation of Ni-YSZ Electrodes in Solid Oxide Cells: Impact of Polarization and Initial Microstructure on the Ni Evolution. Journal of The Electrochemical Society 2019; 166: F1229.

[22] Liu Q, Zhang Q, Voorhees PW, Barnett SA. Effect of direct-current operation on the electrochemical performance and structural evolution of Ni-YSZ electrodes. Journal of Physics: Energy 2019; 2: 014006.

[23] Li Q, Liang L, Gerdes K, Chen LQ. Phase-field modeling of three-phase electrode microstructures in solid oxide fuel cells. Applied Physics Letters 2012; 101: 033909.

[24] Zhu J, Lin Z. Degradations of the electrochemical performance of solid oxide fuel cell induced by material microstructure evolutions. Applied Energy 2018; 231: 22-28.

[25] Jiao Z, Shikazono N. Prediction of nickel morphological evolution in composite solid oxide fuel cell anode using modified phase field model. Journal of The Electrochemical Society 2018; 165: F55.

[26] Jiao Z, Shikazono N. Study on the effects of polarization on local morphological change of nickel at active three-phase-boundary using patterned nickel-film electrode in solid oxide fuel cell anode. Acta Materialia 2017; 135: 124-131.

[27] Jiao Z, Busso EP, and Shikazono N. Influence of polarization on the morphological changes of nickel in fuel electrodes of solid oxide cells. Journal of the Electrochemical

Society 2020; 167.2: 024516.

[28] Menzler NH, Sebold D, Sohn YJ, Zischke S. Post-test characterization of a solid oxide fuel cell after more than 10 years of stack testing. Journal of Power Sources 2020; 478: 228770.

[29] Lei, Y., Cheng, T. L., & Wen, Y. H. (2017). Phase field modeling of microstructure evolution and concomitant effective conductivity change in solid oxide fuel cell electrodes. Journal of Power Sources, 345, 275-289.

[30] Mohamad AA. Lattice Boltzmann Method. Vol. 70. London: Springer, 2011.

[31] Shikazono N, Kanno D, Matsuzaki K, Teshima H, Sumino S, Kasagi N. Numerical assessment of SOFC anode polarization based on three-dimensional model microstructure reconstructed from FIB-SEM images. Journal of The Electrochemical Society 2010; 157: B665.

[32] Wang Y, Du Y, Ni M, Zhan R, Du Q, Jiao K. Three-dimensional modeling of flow field optimization for co-electrolysis solid oxide electrolysis cell. Applied Thermal Engineering 2020; 172: 114959.

[33] Wang Y, Zhan R, Qin Y, Zhang G, Du Q, Jiao K. Three-dimensional modeling of pressure effect on operating characteristics and performance of solid oxide fuel cell. International Journal of Hydrogen Energy 2018; 43: 20059-20076.

[34] Wilson JR, Cronin JS, Duong AT, Rukes S, Chen HY, Thornton K, et al. Effect of composition of (La0. 8Sr0. 2MnO3–Y2O3-stabilized ZrO2) cathodes: Correlating three-dimensional microstructure and polarization resistance. Journal of Power Sources 2010; 195: 1829-1840.

[35] Mu Y, Chen L, He Y, Tao W. Pore-scale modelling of dynamic interaction between SVOCs and airborne particles with lattice Boltzmann method. Building and Environment 2016; 104: 152-161.

[36] Mu Y, Weber AZ, Gu ZL, Tao W. Mesoscopic modeling of transport resistances in a polymer-electrolyte fuel-cell catalyst layer: Analysis of hydrogen limiting currents. Applied Energy 2019; 255: 113895.

[37] Chen L, Shen J. Applications of semi-implicit Fourier-spectral method to phase field equations. Computer Physics Communications 1998; 108: 147-158.

[38] Cai Q, Adjiman CS, Brandon NP. Modelling the 3D microstructure and performance of solid oxide fuel cell electrodes: computational parameters. Electrochimica Acta 2011; 56(16): 5804-5814.

[39] Zhang Y, Sun Q, Xia C, et al. Geometric properties of nanostructured solid oxide fuel cell electrodes. Journal of The Electrochemical Society 2013; 160(3): F278.

[40] Ringuede A, Bronine D, Frade JR. Ni1− xCox/YSZ cermet anodes for solid oxide fuel cells. Electrochimica Acta 2002; 48: 437-442.

[41] Skarmoutsos D, Nikolopoulos P, Tsoga A. Titania doped YSZ for SOFC anode Ni-Cermet. Ionics 1999; 5: 455-459.

[42] Zhang W, Chen M, Kuhn LT, Bowen JR, Bentzen JJ. Electrochemistry Unlocks Wettability: Epitaxial Growth of Oxide Nanoparticles on Rough Metallic Surfaces. ChemElectroChem 2014; 1.3: 520-523.

[43] Fang Q, Frey CE, Menzler NH, Blum L. Electrochemical performance and preliminary

post-mortem analysis of a solid oxide cell stack with 20,000 h of operation. Journal of The Electrochemical Society 2018; 165: F38.